*J. Fluid Mech.* (2024), *vol*. 987, A14, doi:10.1017/jfm.2024.368

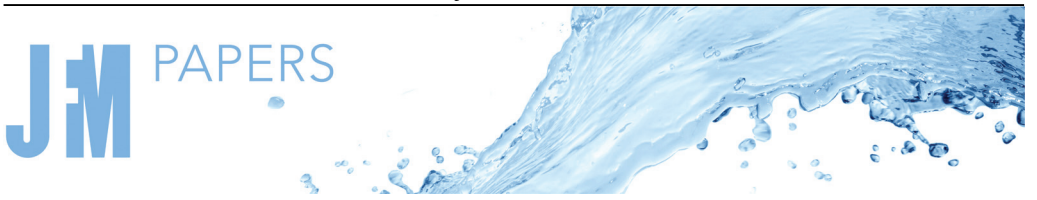

# Unifying constitutive law of vibroconvective turbulence in microgravity

**Ze-Lin Huang[1], Jian-Zhao Wu[1,2,†], Xi-Li Guo[1], Chao-Ben Zhao[1], Bo-Fu Wang[1], Kai Leong Chong[1,2] and Quan Zhou[1,†]**

[1]Shanghai Key Laboratory of Mechanics in Energy Engineering, Shanghai Institute of Applied Mathematics and Mechanics, School of Mechanics and Engineering Science, Shanghai University, Shanghai 200072, PR China

[2]Shanghai Institute of Aircraft Mechanics and Control, Zhangwu Road, Shanghai 200092, PR China

(Received 16 November 2023; revised 8 April 2024; accepted 8 April 2024)

We report the unified constitutive law of vibroconvective turbulence in microgravity, i.e. $Nu \sim a^{-1}Re_{os}^{\beta}$ where the Nusselt number $Nu$ measures the global heat transport, $a$ is the dimensionless vibration amplitude, $Re_{os}$ is the oscillational Reynolds number and $\beta$ is the universal exponent. We find that the dynamics of boundary layers plays an essential role in vibroconvective heat transport and the $Nu$-scaling exponent $\beta$ is determined by the competition between the thermal boundary layer (TBL) and vibration-induced oscillating boundary layer (OBL). Then a physical model is proposed to explain the change of scaling exponent from $\beta = 2$ in the TBL-dominant regime to $\beta = 4/3$ in the OBL-dominant regime. Our finding elucidates the emergence of universal constitutive laws in vibroconvective turbulence, and opens up a new avenue for generating a controllable effective heat transport under microgravity or even microfluidic environment in which the gravity effect is nearly absent.

**Key words:** convection

## 1. Introduction

The emergence of a unified constitutive law is a hallmark of gravity-induced convective turbulence (Ahlers, Grossmann & Lohse 2009; Sreenivasan 2019; Wang, Mathai & Sun 2019; Chen, Wang & Xi 2020; Jiang *et al.* 2020; Wang *et al.* 2021; Li *et al.* 2022; Zhao *et al.* 2022; Ecke & Shishkina 2023), e.g. $Nu \sim Ra^{\beta}$ with $\beta \approx 0.3$ in the classical regime (Ahlers *et al.* 2009; Huang & Zhou 2013; Xi *et al.* 2016; Zhang, Zhou & Sun 2017; Plumley & Julien 2019; Iyer *et al.* 2020; Ahlers *et al.* 2022; Xu, Xu & Xi 2023; Li, Chen & Xi 2024) and $\beta = 1/2$ in the ultimate regime for paradigmatic Rayleigh–Bénard (RB) convection

† Email addresses for correspondence: jianzhao_wu@shu.edu.cn, qzhou@shu.edu.cn

(Grossmann & Lohse 2011; He *et al.* 2012; Toppaladoddi, Succi & Wettlaufer 2017; Lepot, Aumaître & Gallet 2018; Wang, Zhou & Sun 2020; Zou & Yang 2021; Jiang *et al.* 2022), where the Nusselt number $Nu$ quantifies the heat transport efficiency and the Rayleigh number $Ra$ quantifies the strength of buoyancy forcing. However, in microgravity, as the gravity effect is, however, almost absent, gravity-induced convection becomes too feeble to transport matter and heat. Vibration, omnipresent in science and technology, has been shown to be an attractive way to operate fluids, modulate convective patterns and control heat transport by creating an 'artificial gravity' (Beysens *et al.* 2005; Beysens 2006), e.g. vibration shapes liquid interfaces in an arbitrary direction (Gaponenko *et al.* 2015; Sánchez *et al.* 2019, 2020; Apffel *et al.* 2021), vibration levitates a fluid layer upon a gas layer (Apffel *et al.* 2020), vibration selects patterns through the parametric response (Rogers *et al.* 2000*a*,*b*; Pesch *et al.* 2008; Salgado Sánchez *et al.* 2019), vibration significantly enhances or suppresses heat transport depending on the mutual direction of vibration and temperature gradient (Swaminathan *et al.* 2018; Wang *et al.* 2020; Wu *et al.* 2021, 2022*a*; Guo *et al.* 2022; Wu, Wang & Zhou 2022*b*). Vibroconvection, resulting directly from a non-isothermal fluid subjected to the external vibration, is very pronounced under microgravity conditions and provides a potential mechanism of heat and mass transport in the absence of gravity-induced convection (Gershuni & Lyubimov 1998; Mialdun *et al.* 2008; Shevtsova *et al.* 2010). Elucidating the potential constitutive law of vibroconvective turbulence and its underlying mechanism is not only of great importance in microgravity science, but also provides practical guiding significance for space missions (Monti, Savino & Lappa 2001) and microfluidic technologies (Daniel, Chaudhury & De Gennes 2005; Brunet, Eggers & Deegan 2007).

In past decades, due to the difficulty of conducting microgravity experiments, the experimental studies on vibroconvection at low gravity were limited. An experiment was carried out with the ALICE-2 instrument onboard the Mir space station, which revealed the vibrational influence on the propagation of a temperature wave from a heat source in near-critical fluids (Zyuzgin *et al.* 2001; Garrabos *et al.* 2007). The other known experiment was conducted in the parabolic flights during the 46th campaign organized by the European Space Agency, which reported the first direct experimental evidence of vibroconvection in low gravity (Mialdun *et al.* 2008; Shevtsova *et al.* 2010). There are extensive theoretical and numerical investigations of vibroconvection under weightlessness conditions. In the limiting case of high-frequencies and small amplitudes, the averaging technique was applied to theoretically deduce the dynamical equation of the mean flows (Gershuni & Lyubimov 1998). Based on the averaged equations, the onset and bifurcation scenarios of vibroconvection were widely investigated in square, rectangular and cubic enclosures (Savino, Monti & Piccirillo 1998; Cissé, Bardan & Mojtabi 2004). The synchronous, subharmonic and non-periodic responses to external vibration were observed in vibroconvection from a parametric study over a wide range of frequencies and amplitudes (Hirata, Sasaki & Tanigawa 2001; Crewdson & Lappa 2021). The parametric and Rayleigh-vibrational instability were examined in vibroconvection in the absence of gravity (Amiroudine & Beysens 2008; Sharma *et al.* 2019). The heat transport enhancement near the onset of vibroconvection were also investigated (Gershuni & Lyubimov 1998; Shevtsova *et al.* 2010). However, the basic properties of constitutive law in vibroconvective turbulence have been rarely addressed.

In this paper, we carried out a series of direct numerical simulations on vibroconvection in a wide range of vibration amplitudes and frequencies. Then we theoretically and numerically unveil the emergence of a unified constitutive law and underlying mechanism of vibroconvective turbulence. In § 2, the governing equations and numerical approach

of microgravity vibroconvection are described. In § 3, flow structure in vibroconvection is analysed and the unified scaling law of vibroconvective heat transport is revealed theoretically and examined numerically. Finally, the conclusion is given in § 4.

## 2. Direct numerical simulation

We consider the microgravity vibroconvection set-up of the convective flows in an enclosure heated from below by a hot wall and cooled from above by a cold wall, and subjected to the harmonic vibration $A\cos(\Omega t)$ in the horizontal direction. Here, $\Omega$ and $A$ are the angular frequency and pulsating displacement. In the non-inertial frame associated with the imposed vibration, an inertial acceleration of $A\Omega^2\cos(\Omega t)\boldsymbol{e}_x$ is added to the system, where $\boldsymbol{e}_x$ is the unit vector in the $x$-direction. The governing equations for vibroconvective turbulence can then be written as

$$\partial_t \boldsymbol{u} + (\boldsymbol{u}\cdot\boldsymbol{\nabla})\boldsymbol{u} = -\boldsymbol{\nabla} p + \nu\nabla^2\boldsymbol{u} - \alpha A\Omega^2\cos(\Omega t)T\boldsymbol{e}_x, \tag{2.1}$$

$$\partial_t T + (\boldsymbol{u}\cdot\boldsymbol{\nabla})T = \kappa\nabla^2 T, \tag{2.2}$$

in addition to $\boldsymbol{\nabla}\cdot\boldsymbol{u} = 0$, where $\boldsymbol{u}$ is the fluid velocity, $T$ the temperature, $p$ the modified pressure, $\nu$ the kinematic viscosity, $\kappa$ thermal diffusivity and $\alpha$ thermal expansion coefficient, respectively. Here, the modified pressure is expressed as $p = \tilde{p} - \alpha A\Omega^2\cos(\Omega t)T_0 x$ where $\tilde{p}$ is the fluid pressure and $T_0$ is the reference temperature (Shevtsova *et al.* 2010). All quantities used in our simulations have been made dimensionless with respect to the cell's height $H$, the temperature difference across the fluid layer $\Delta$ and the viscous diffusion velocity $\nu/H$. Based on these choices, the relevant control parameters for the vibroconvection system are the dimensionless vibration amplitude $a = \alpha\Delta A/H$, the dimensionless vibration frequency $\omega = \Omega H^2/\nu$ and the Prandtl number $Pr = \nu/\kappa$.

We performed direct numerical simulation of microgravity vibroconvection in a rectangular enclosure with aspect ratio of $W : D : H = 1 : 0.3 : 1$ in three-dimensional (3-D) cases and of $W : H = 1 : 1$ in two-dimensional (2-D) cases, where $W$, $D$, $H$ are, respectively, the width, depth and height of the convection cell. The governing equations are numerically solved by a second-order finite difference code, which has been validated many times in the single-phase turbulent convection (Zhang *et al.* 2018; Wang *et al.* 2020; Guo *et al.* 2022, 2023; Wu *et al.* 2022*a*,*b*; Huang *et al.* 2023; Chong *et al.* 2024; Zhang & Zhou 2024) and multiphase flow (Meng *et al.* 2024; Zhao *et al.* 2024). Furthermore, the comparison between our simulation results and experimental data reported in Shevtsova *et al.* (2010) is given in Appendix A. The agreement on the growth of the heat flux validates our in-house code. At all solid boundaries, no-slip boundary conditions are applied for the velocity. At the top and bottom plates, the dimensionless temperature is adopted as constant $T_{top} = 0$ and $T_{bot} = 1$; and at all sidewalls, the adiabatic conditions are adopted. We performed a series of direct numerical simulations of microgravity vibroconvective turbulence over the vibration amplitude range $0.001 \le a \le 0.1$ and the frequency range $10^5 \le \omega \le 10^7$ for 3-D cases, and over the vibration amplitude range $0.001 \le a \le 0.3$ and the frequency range $10^3 \le \omega \le 10^7$ for 2-D cases at fixed Prandtl number $Pr = 4.38$. For all simulations, the computational mesh size is chosen to adequately resolve the dynamics both the thermal and oscillating boundary layers (BLs), and the time step is chosen to not only fulfil the Courant–Friedrichs–Lewy conditions, but also resolve the time scale of 1 % of the vibration period.

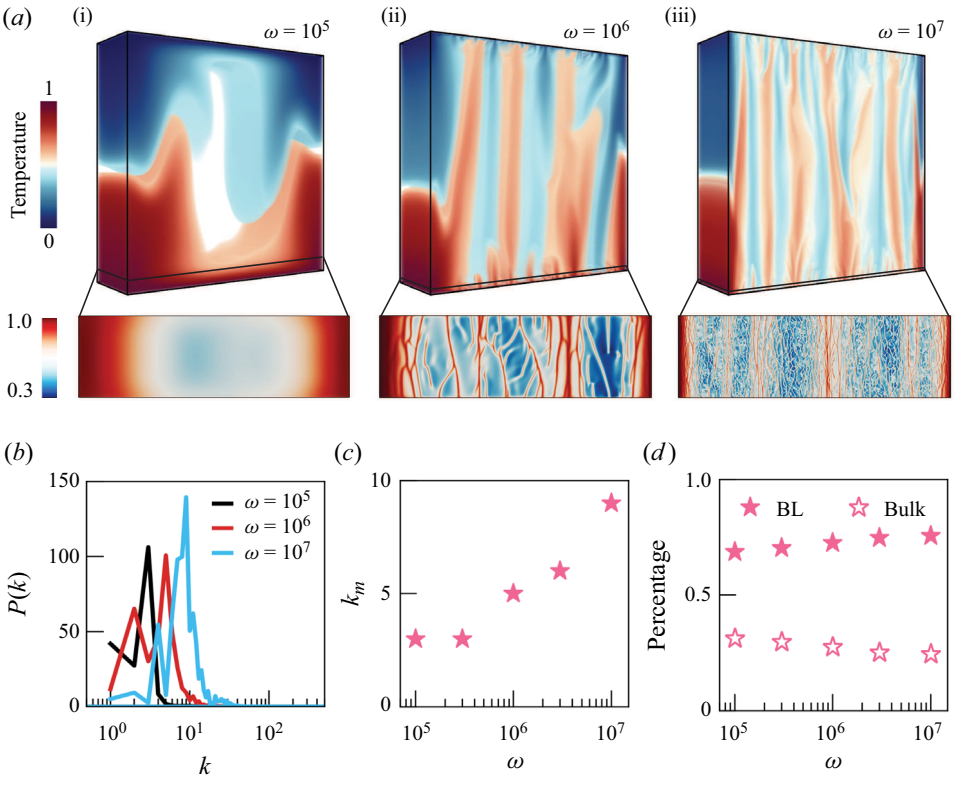


Figure 1. Flow structure in microgravity vibroconvection. (*a*) Instantaneous 3-D flow structure visualized by the volume rendering of the instantaneous temperature field (see supplementary movies available at https://doi.org/10.1017/jfm.2024.368) under different vibration frequencies $\omega = 10^5$ (*a* i), $10^6$ (*a* ii) and $10^7$ (*a* iii) at fixed amplitude $a = 0.01$ and Prandtl number $Pr = 4.38$. The subpanels below show the corresponding temperature contours extracted on the horizontal slice at the edge of TBL. (*b*) Power spectrum of fluctuating temperature in bulk zones. (*c*) The variation of the characteristic wavenumber $k_m$ as functions of $\omega$. (*d*) Percentage of BL (solid symbols) and bulk (hollow symbols) to the global averaged thermal dissipation rate, as functions of vibration frequency.

## 3. Results and discussion

Figure 1(*a*) shows the typical snapshots of flow structures in vibroconvection with different dimensionless frequencies $\omega = 10^5$, $10^6$ and $10^7$ at fixed dimensionless amplitude $a = 0.01$ and fixed Prandtl number $Pr = 4.38$. It is seen that the shaking by external vibration strongly destabilizes the conductive state and generates large distortion of the temperature field in bulk regions by creating an artificial gravity (Beysens *et al.* 2005; Beysens 2006). With increasing $\omega$, it is vibration-induced artificial gravity that becomes strong enough to destabilize the TBL and trigger abundant thermal plumes. Those plumes are transported into bulk regions and self-organized into columnar structures. This indicates that the feature of the main structures responsible for heat transport in microgravity vibroconvection are different from those in the gravity-induced RB convection. The vertical columnar structure in the bulk is very similar to the columnar pattern observed in experiments on the interface between two miscible liquids under vibration in microgravity (Gaponenko *et al.* 2015).

To quantitatively analyse the feature of columnar structures, we extract the instantaneous temperature field in bulk zones and calculate the power spectrum $P(k)$ of temperature

fluctuations by applying the Fourier transform in the vibrational direction as shown in figure 1(*b*). It is found that there exists a characteristic wavenumber $k_m$, at which the wavenumber distribution function $P(k)$ is maximal. Indeed, $k_m$ characterizes the number of columnar structures in vibroconvection. We then plot the variation of $k_m$ as functions of $\omega$ in figure 1(*c*). It is shown that $k_m$ monotonically increases with increasing $\omega$, indicating that more columnar structures are formed under a stronger vibrational driving force. Such a kind of relation for the columnar structures was experimentally established while vibrating two miscible liquids (see figure 5 in the work of Gaponenko *et al.* (2015)). This is consistent with the fact that larger heat transport enhancement occurs at larger $\omega$. Further, to examine the role of the TBL in vibroconvective heat transport processes, we decompose the globally averaged thermal dissipation rate $\epsilon_T = \kappa|\nabla T|^2$ into their boundary layer (BL) and bulk contributions, and then plot the variation of relative contributions as functions of $\omega$ in figure 1(*d*), as suggested by the Grossmann–Lohse theory (Ahlers *et al.* 2009; Stevens *et al.* 2013). It is seen in figure 1(*d*) that the BL contribution of $\epsilon_T$ is much larger than the bulk one, suggesting the BL-dominant thermal dissipation. This reveals that the dynamics of BLs plays a crucial role on the underlying mechanism of heat transport in vibroconvective turbulence.

Next, we address the question of how the global heat transport depends on the control parameters of vibroconvection. First, we examine the dependence of heat transport on the vibration frequency. Figure 2(*a*,*d*) shows the measured $Nu$ as functions of frequency $\omega$ in a log–log plot for different amplitudes $a$ in 3-D and 2-D cases. Here, the $Nu$ number, as the non-dimensional ratio of the measured heat flux to the conductive one, is calculated by $Nu = \langle wT - \kappa\partial_z T\rangle/(\kappa\Delta/H)$, where $w$ is the vertical velocity and $\langle\cdot\rangle$ denotes the time and space averaging. It is observed that the $Nu$–$\omega$ scaling relation is not unique for a specific amplitude, namely, there seems to be a transition from $Nu \sim \omega$ to $Nu \sim \omega^{2/3}$ in both 3-D and 2-D cases, as shown by the dashed lines or in figure 5 in Appendix B. Note that the precise values of scaling exponents are obtained from the physical model we proposed below, not adjusted from the fitting with the numerical data.

Further, we examine the dependency of heat transport on the two important analogous Rayleigh numbers in vibroconvective turbulence, which are the vibrational Rayleigh number $Ra_{vib}$ and oscillational Rayleigh number $Ra_{os}$. The first one is the vibrational Rayleigh number $Ra_{vib} = (\alpha A\Omega\Delta H)^2/(2\nu\kappa)$, i.e. $Ra_{vib} = \frac{1}{2}a^2\omega^2 Pr$, which is obtained from applying the averaged approach on vibroconvective equations in the limit of small amplitudes and high frequencies, and quantifies the intensity of the external vibrational source. Figure 2(*b*,*e*) depict, respectively, the measured $Nu$ as functions of $Ra_{vib}$ in a log–log plot at different amplitudes for 3-D and 2-D cases. We find that at small $Ra_{vib}$, numerical data almost collapse together on the same scaling law, i.e. $Nu \sim Ra_{vib}^{1/2}$, as shown by the dashed lines. However, at large $Ra_{vib}$, a significant departure from this scaling behaviour is observed for large amplitudes. The other is the oscillational Rayleigh number $Ra_{os} = \alpha A\Omega^2\Delta H^3/(\nu\kappa)$, i.e. $Ra_{os} = a\omega^2 Pr$, which is analogous to Rayleigh number in RB convection but replacing the gravitation by the vibration-induced acceleration. Figure 2(*c*,*f*) shows the variation of $Nu$ as functions of $Ra_{os}$ for various amplitudes in 3-D and 2-D cases. We find that at large $Ra_{os}$, numerical data almost collapse onto the same scaling relation $Nu \sim Ra_{os}^{1/3}$ as shown by the dashed line, but at small $Ra_{os}$, numerical data points deviate considerably from this scaling for small amplitudes. Both scaling relations $Nu \sim Ra_{vib}^{1/2}$ for small $Ra_{vib}$ and $Nu \sim Ra_{os}^{1/3}$ for large $Ra_{os}$ can be further confirmed from the compensated plots in figure 6 in Appendix C. From above, using solely

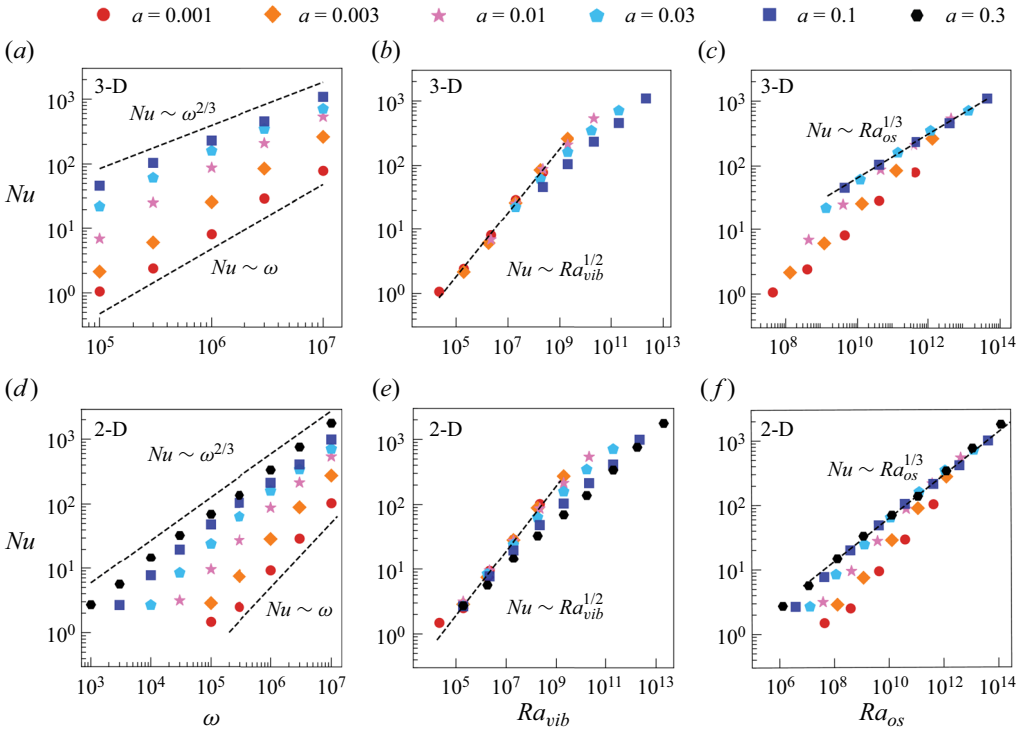


Figure 2. Heat transport scaling in vibroconvective turbulence. (*a–c*) The measured Nusselt number $Nu$ as functions of vibration frequency $\omega$, vibrational Rayleigh number $Ra_{vib}$, oscillational Rayleigh number $Ra_{os}$ for 3-D cases. (*d–f*) The measured Nusselt number $Nu$ as functions of vibration frequency $\omega$, vibrational Rayleigh number $Ra_{vib}$, oscillational Rayleigh number $Ra_{os}$ for 2-D cases. The dashed lines in the panels are $Nu \sim \omega$ (lower), $Nu \sim \omega^{2/3}$ (upper) in (*a*,*d*), $Nu \sim Ra_{vib}^{1/2}$ in (*b*,*e*), $Nu \sim Ra_{os}^{1/3}$ in (*c*,*f*). Those precise scaling relations are theoretically deduced by our proposed physical model in the paper. Note that the vibration amplitude range in the 3-D cases is from $a = 10^{-3}$ to $a = 10^{-1}$ and in the 2-D cases is from $a = 10^{-3}$ to $a = 3 \times 10^{-1}$.

the common control parameters like $\omega$, $Ra_{vib}$ or $Ra_{os}$, unifying the heat transport scaling in vibroconvective turbulence cannot be achieved.

Now, there are two important questions remaining to be answered in vibroconvective turbulence: one is why there exists two different heat transport scaling laws, i.e. $Nu \sim Ra_{vib}^{1/2}$ and $Nu \sim Ra_{os}^{1/3}$; the other is whether a unified constitutive law emerges in vibroconvective turbulence. Hereafter, we propose a physical model to address the first question. From the analysis above, we know that the BL-contribution to the global thermal dissipation rate is dominant, implying that the BL dynamics plays a crucial role in the heat transport mechanism. In vibroconvective turbulence, there are two types of BL: the thermal boundary layer (TBL) with the thickness of $\delta_{th}$, which is estimated by $\delta_{th} \approx H/(2Nu)$; the other is the oscillating boundary layer (OBL) induced by the external vibration. The modulation depth of OBL referring to $\delta_{os}$ is defined as the depth, at which the delaying rate of the intensity of vibration-induced shear effect is equal to 99 %. Considering the intensity of vibrational modulation falling off exponentially from the surface, one easily obtains $\delta_{os} = -\ln(1-0.99)\delta_S \approx 4.605\delta_S$ where $\delta_S = \sqrt{2\nu/\Omega}$ is the Stokes layer thickness. First, when $\delta_{th} > \delta_{os}$ as sketched in figure 3(*ai*), by taking into account the balance between the convective and conductive transports within TBL, the dimensional analysis of the governing equation of the temperature field gives

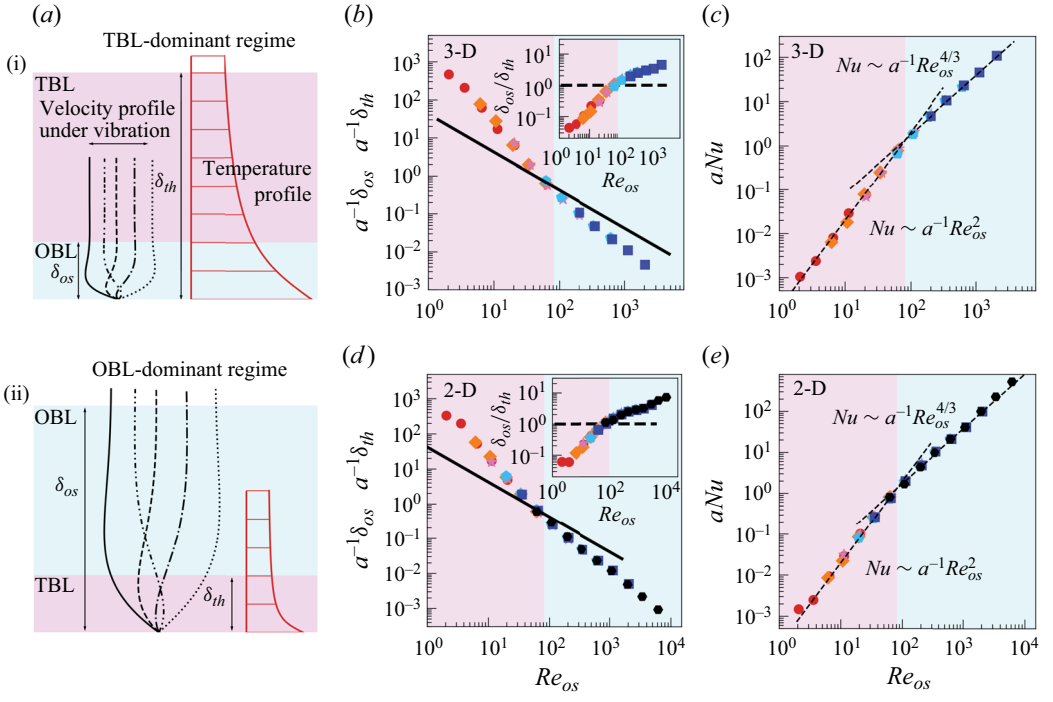


Figure 3. Unified constitutive law in vibroconvective turbulence. (*a*) Sketch of the (*a* i) TBL-dominant regime and the (*a* ii) OBL-dominant regime. (*b*,*d*) The TBL thickness $\delta_{th}$ (symbols) and the critical modulation depth $\delta_{os}$ (solid line) of OBL as a function of the oscillational Reynolds number $Re_{os}$ for 3-D and 2-D cases. The insets in (*b*,*d*) show the ratio $\delta_{os}/\delta_{th}$ as a function of the oscillational Reynolds number $Re_{os}$. The solid dashed line indicates $\delta_{os}/\delta_{th} = 1$. (*d*,*e*) The unified scaling law exhibited between $aNu$ and the oscillational Reynolds number $Re_{os}$ for 3-D and 2-D cases. The emergence of a universal constitutive law of vibroconvective turbulence is clearly observed. Here, the TBL-dominated regime is coloured light purple and OBL-dominated regime light cyan in (*b*–*e*). The coloured symbols have the same meaning as those in figure 2.

rise to $w\Delta/\delta_{th} \sim \kappa\Delta/\delta_{th}^2$. And, in the momentum equation, the balance between the vibration-induced buoyancy and the viscous dissipation leads to $\alpha A\Omega^2\Delta \sim \nu u/\delta_{os}^2$ with $u$ the horizontal velocity. Using both above relations, assuming that the magnitude of velocity components $u$ and $w$ follows a similar scaling behaviour, i.e. the ratio $w/u$ is approximately constant, together with $\delta_{os} \sim \sqrt{\nu/\Omega}$ and $\delta_{th} \sim H/Nu$, one obtains the scaling relation between $Nu$ and $Ra_{vib}$,

$$Nu \sim Ra_{vib}^{1/2} Pr^{1/2}. \tag{3.1}$$

The scaling relation in (3.1) shows that vibroconvective heat transport is independent of viscosity $\nu$, but depends on thermal diffusion coefficient $\kappa$. This implies that the dynamics of TBL is dominant to heat transport in cases of $\delta_{th} > \delta_{os}$.

When $\delta_{th} < \delta_{os}$ as sketched in figure 3(*a* ii), the balance between the vibration-induced buoyancy and the viscous dissipation within TBL allows one to rewrite the momentum equation using dimensional analysis: $\alpha A\Omega^2\Delta \sim \nu u/\delta_{th}^2$. Combining the above equation and $w\Delta/\delta_{th} \sim \kappa\Delta/\delta_{th}^2$ for the temperature equation, together with the above assumption that the ratio $w/u$ is approximately constant, $\delta_{os} \sim \sqrt{\nu/\Omega}$ and $\delta_{th} \sim H/Nu$, one deduces the scaling relation between $Nu$ and $Ra_{os}$,

$$Nu \sim Ra_{os}^{1/3}. \tag{3.2}$$

The heat transport scaling in (3.2) is similar to that of RB convection in the classical regime through replacing the gravitation by vibration-induced acceleration. Both heat transport scalings predicted in (3.1) and (3.2) agree well with numerical results shown in figure 2. The competition between TBL and OBL results in the two different heat transport scaling relations, namely, $Nu \sim Ra_{vib}^{1/2}$ and $Nu \sim Ra_{os}^{1/3}$.

Furthermore, we address the second question of whether the universal constitutive law of vibroconvective turbulence emerges. First, to quantify the dynamics of OBL, we define the oscillational Reynolds number $Re_{os} = \alpha \Delta A \Omega \delta_{os}/\nu$, which is related to the vibrational velocity with the Boussinesq parameter $\alpha \Delta A \Omega$ and the modulation depth $\delta_{os}$ and obeys the relation $Re_{os} = 4.605a(2\omega)^{1/2}$. Second, we study the dependency of $Nu$ on $Re_{os}$. It is intriguing to find that both $Nu \sim Ra_{vib}^{1/2}$ and $Nu \sim Ra_{os}^{1/3}$ scaling laws can be rewritten as $Nu \sim a^{-1}Re_{os}^{\beta}$ with $\beta = 2$ for the TBL-dominant heat transport regime ($\delta_{th} > \delta_{os}$), and $\beta = 4/3$ for the OBL-dominant heat transport regime ($\delta_{th} < \delta_{os}$). Therefore, we conclude that due to the competition between the dynamics TBL and OBL on heat transport, the underlying mechanism of heat transport in vibroconvective turbulence can be categorized into the two following regimes.

(i) The TBL-dominant regime ($\delta_{th} > \delta_{os}$): the OBL is submerged into TBL. Thermal plumes facilitated by vibration-induced strong shear detach from OBL and move into TBL. The plume dynamics is then mainly dominant by the molecular diffusion between OBL and TBL. Those plumes thermally diffuse and then self-organize into columnar structures in bulk zones, which transport heat from the bottom hot plate to the top cold one. The heat transport scaling exhibits the scaling $Nu \sim a^{-1}Re_{os}^{2}$.

(ii) The OBL-dominant regime ($\delta_{os} > \delta_{th}$): the TBL is nested into OBL. The OBL dominates the dynamics of thermal plumes ejected from TBL by vibration-induced strong shear. Between OBL and TBL, the shear effect mixes those plumes and sweep away some of them (Scagliarini, Gylfason & Toschi 2014; Blass *et al.* 2020; Jin *et al.* 2022). The remaining plumes then move into bulk zones and self-organize into columnar structures. In this regime, due to the plume-sweeping mechanism between OBL and TBL, the heat transport is depleted and obeys the scaling with a smaller scaling relation exponent $Nu \sim a^{-1}Re_{os}^{4/3}$.

Finally, we use the simulated data to confirm the theoretically deduced unified constitutive law. First, we plot in figure 3(*b*,*d*) the variation of both $a\delta_{th}$ and $a\delta_{os}$ as functions of $Re_{os}$. It is shown that for all fixed amplitudes, the value of both $\delta_{th}$ and $\delta_{os}$ monotonically decreases as increasing $Re_{os}$, and $\delta_{th}$ decreases faster than $\delta_{os}$. The intersection point between the curves of $a\delta_{th}$ and $a\delta_{os}$ divides the plane into two regions, which corresponds to the TBL-dominant regime in the left-hand side ($\delta_{th} > \delta_{os}$) and OBL-dominant regime in the right-hand side ($\delta_{th} > \delta_{os}$). As depicted in the inset of figure 3(*b*,*d*), the dividing line between TBL-dominant and OBL-dominant regimes is nearly at the position of $\delta_{os}/\delta_{th} = 1$. This confirms that the underlying mechanism of vibroconvective heat transport is attributed to the competition between the dynamics of TBL and OBL. Second, we plot the calculated $aNu$ as functions of $Re_{os}$ as shown in figure 3(*c*,*e*). It is expected that all numerical data collapse together onto the derived universal constitutive law. Evidently, the numerical data and theoretical model show an excellent agreement. This confirms the emergence of the universal constitutive law of vibroconvective turbulence in microgravity. The evidence of this unified heat transport heat scaling is also shown from the compensated plots in figure 7 in Appendix D.

## 4. Conclusions

In summary, we have conducted direct numerical simulations of both 2-D and 3-D microgravity vibroconvective turbulence over a wide range of dimensionless vibration amplitude and frequency at fixed $Pr = 4.38$. It is shown that in the absence of gravitational acceleration, vibration creates an 'artificial gravity' in microgravity to destabilize TBL and trigger a massive eruption of thermal plumes. We find that those plumes are finally self-organized into columnar structures in bulk zones to transport heat from the bottom hot plate to the top cold one. This is different from the gravity-induced convection, like RB convection, in which large-scale circulation is formed in the bulk and dominates heat transport. By analysing the basic properties of heat transport, we find the heat transport exhibits two different power-low relations, i.e. $Nu \sim Ra_{vib}^{1/2}$ at small amplitudes and $Nu \sim Ra_{os}^{1/3}$ at large amplitudes. Both $Nu$-relations show that the global heat flux is independent of the cell height. We also find that the BL-contribution is dominant to the global thermal dissipation rate, implying that the dynamics of BL plays an essential role in vibroconvective heat transport. We then propose a physical model to theoretically deduce both $Nu$-scaling-relations, and explain the distinct properties of vibroconvective heat transport, based on the competition between the TBL and OBL induced by the external vibration. To look for the universal features, we define the oscillational Reynolds number $Re_{os}$ quantifying the dynamics of OBL, and study the dependency of heat transport on $Re_{os}$. Both theoretical results and numerical data shows the emergence of the universal constitutive law in vibroconvective turbulence, i.e. $Nu \sim a^{-1}Re_{os}^{\beta}$, where $\beta$ is the universal scaling exponent. We also find that the exponent $\beta$ is determined by the relative importance between the dynamics of TBL and of OBL to heat transport, and identify $\beta = 2$ in TBL-dominant regime and $\beta = 4/3$ in OBL-dominant regime. It is concluded that the type of vibroconvective turbulence in microgravity owns a universal constitutive law with its underlying heat transport mechanism different from that in gravity-induced convective turbulence. The emergence of universal constitutive laws in vibroconvective turbulence provides a powerful basis for generating a controllable heat transport under microgravity conditions or in a microfluidic environment.

**Supplementary movies.** Supplementary movies are available at https://doi.org/10.1017/jfm.2024.368.

**Funding.** This work was supported by the Natural Science Foundation of China under grant nos. 11988102, 92052201, 12032016, 12102246 and 11972220.

**Declaration of interests.** The authors report no conflict of interest.

**Author ORCIDs.**
Jian-Zhao Wu https://orcid.org/0000-0002-7981-3623;
Bo-Fu Wang https://orcid.org/0000-0001-6488-6275;
Kai Leong Chong https://orcid.org/0000-0002-3182-3689;
Quan Zhou https://orcid.org/0000-0002-0411-7228.

## Appendix A. Comparison with the experimental results

To further validate our simulation, we compared our simulated Nusselt number with the experimentally measured data in parabolic flight reported in Shevtsova *et al.* (2010). Note that in the validation case, a linear temperature profile is applied on the lateral boundaries and the residual gravity also remained, which is different from the fact that lateral boundaries are adiabatic and the gravity vanishes in the main text. The main

| $A$ (m) | $\Omega$ (Hz) | $\nu$ (m$^2$ s$^{-1}$) | $\kappa$ (m$^2$ s$^{-1}$) | $\Delta$ (K) | $\alpha$ (K$^{-1}$) | $g_x$ (m s$^{-2}$) | $g_y$ (m s$^{-2}$) | $g_z$ (m s$^{-2}$) |
|---|---|---|---|---|---|---|---|---|
| 0.045 | $8\pi$ | $1.730 \times 10^{-6}$ | $0.623 \times 10^{-7}$ | 20 | $1.095 \times 10^{-3}$ | $0.001g$ | $0.001g$ | $0.02g$ |
| $a$ | $\omega$ | $Pr$ | $Ra_{vib}$ | $Ra_{os}$ | $Re_{os}$ | $Ra_x$ | $Ra_y$ | $Ra_z$ |
| $1.971 \times 10^{-1}$ | 363.005 | 27.769 | $7.115 \times 10^5$ | $7.220 \times 10^5$ | 24.456 | 2491.661 | 2491.661 | 4983.322 |

Table 1. Numerical parameters for the validation case. The dimensional cell size is $H = 0.005$ m. The magnitude of gravitation is $g = 9.81$ m s$^{-2}$. The Rayleigh numbers corresponding to the residual gravity are given by $Ra_x = \alpha g_x \Delta H^3/(\nu\kappa)$, $Ra_y = \alpha g_y \Delta H^3/(\nu\kappa)$ and $Ra_z = \alpha g_z \Delta H^3/(\nu\kappa)$. Note that the direction of the residual gravity is the same as with that in Shevtsova *et al.* (2010).

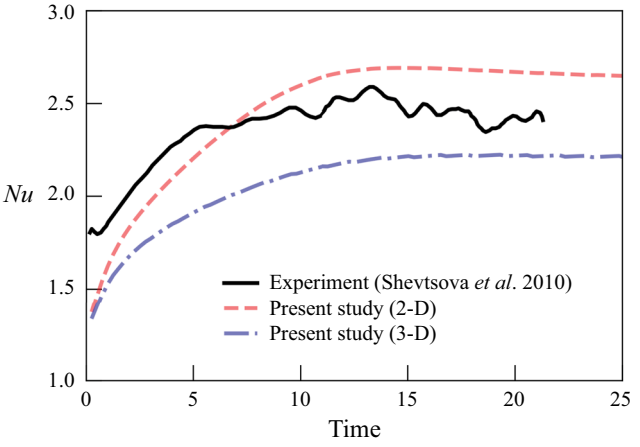


Figure 4. Comparison between the time series of the simulated Nusselt number and experimentally measured data in the parabolic flight reported in the work of Shevtsova *et al.* (2010). Here, the horizontal axis is denoted by the dimensional time.

numerical control parameters are given in table 1. More details of set-up are given in Melnikov *et al.* (2008) and Shevtsova *et al.* (2010). Both the time series of simulated Nusselt number and the experimentally measured one are shown in figure 4. Here, the simulated Nusselt number is calculated using the summation of the normal gradient of the instantaneous temperature over the whole boundaries. The instantaneous temperature field of thermal vibrational convection is extracted at the time of integer multiples of the vibration period. It is shown in figure 4 that the general trend in the growth of the Nusselt number is the same in 2-D/3-D simulations and experiment, although one can see the difference between the value of experimental and numerical results. This result is consistent with the comparison reported in Shevtsova *et al.* (2010). And, Shevtsova *et al.* (2010) reported that this difference is attributed to the different heat flux through the lateral walls between the numerical and experimental set-up.

## Appendix B. Transition from $Nu \sim \omega$ to $Nu \sim \omega^{2/3}$ for fixed $a = 0.03$

To clearly show the transition of scaling relation from $Nu \sim \omega$ to $Nu \sim \omega^{2/3}$, we carried out a series of direct numerical simulations for a fixed amplitude $a = 0.03$ and plot the measured $Nu$ number as a function of $\omega$ in figure 5($a$). A transition from $Nu \sim \omega$ to $Nu \sim \omega^{2/3}$ is observed. And, the compensated plots shown in figure 5($b$,$c$) further confirm this transition of scaling relations.

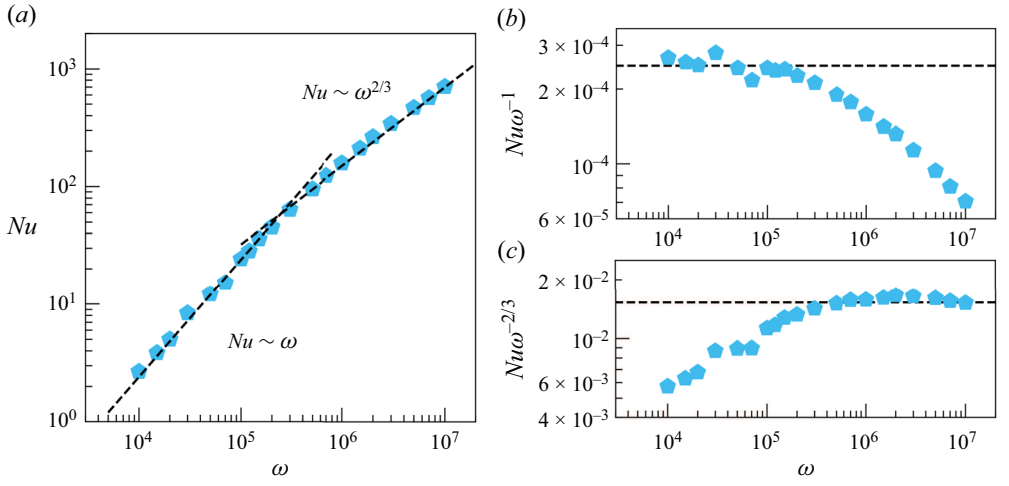


Figure 5. Transition of the $Nu$–$\omega$ relation from $Nu \sim \omega$ to $Nu \sim \omega^{2/3}$ for $a = 0.03$. (*a*) The measured $Nu$ number as a function of vibration frequency $\omega$. (*b*,*c*) The compensated plots of the scaling relations $Nu \sim \omega$ and $Nu \sim \omega^{2/3}$.

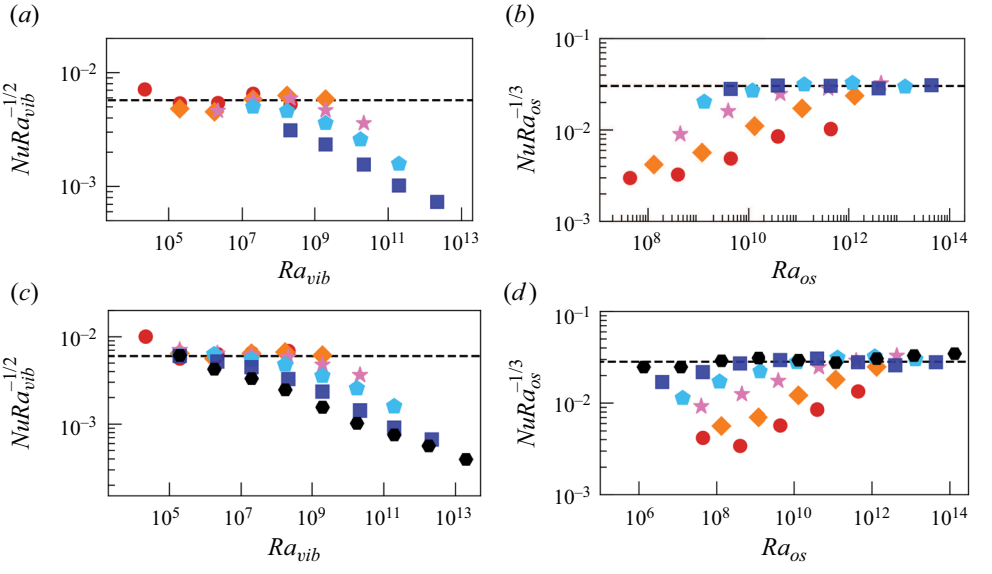


Figure 6. Compensated plots for scaling relations (*a*) $Nu \sim Ra_{vib}^{1/2}$ and (*b*) $Nu \sim Ra_{os}^{1/3}$ for 3-D cases, (*c*) $Nu \sim Ra_{vib}^{1/2}$ and (*d*) $Nu \sim Ra_{os}^{1/3}$ for 2-D cases. Here, the coloured symbols have the same meaning as with those in figure 2.

## Appendix C. Compensated plots for $Nu \sim Ra_{vib}^{1/2}$ and $Nu \sim Ra_{os}^{1/3}$

Figure 6 shows the compensated plots of the heat transport scaling relations $Nu \sim Ra_{vib}^{1/2}$ and $Nu \sim Ra_{os}^{1/3}$ using numerical data of both 3-D and 2-D cases, which correspond to figure 2. Those compensated plots shown in figure 6(*a–d*) further confirm the scaling relations $Nu \sim Ra_{vib}^{1/2}$ and $Nu \sim Ra_{os}^{1/3}$ observed in figure 2.

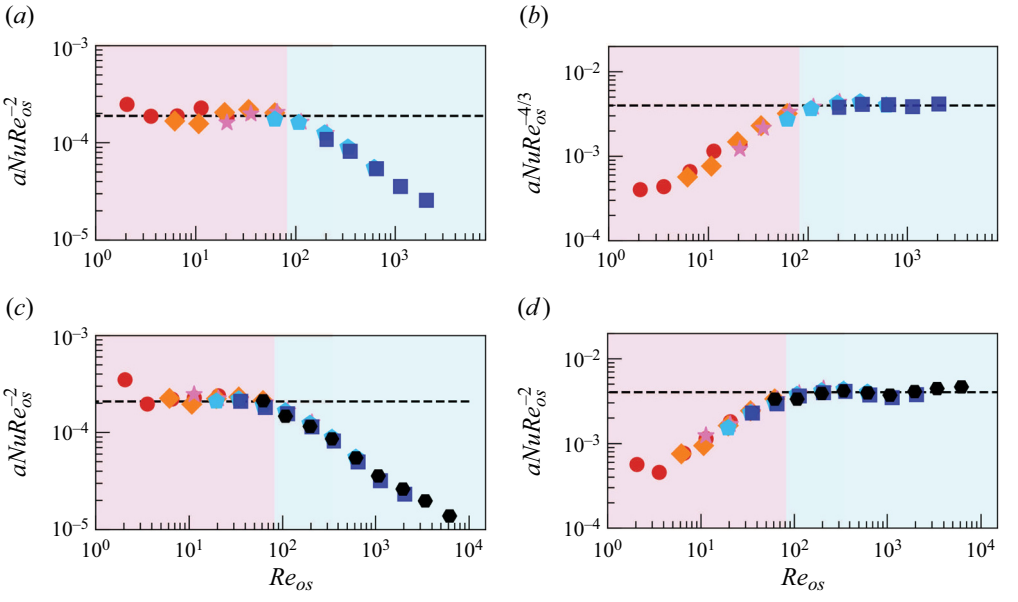


Figure 7. Compensated plots for unified scaling relation (*a*) $Nu \sim a^{-1}Re_{os}^{2}$ and (*b*) $Nu \sim a^{-1}Re_{os}^{4/3}$ for 3-D cases, (*c*) $Nu \sim a^{-1}Re_{os}^{2}$ and (*d*) $Nu \sim a^{-1}Re_{os}^{4/3}$ for 2-D cases. Here, the TBL-dominated regime is coloured light purple and the OBL-dominated regime light cyan in (*a–d*). The coloured symbols have the same meaning as those in figure 2.

## Appendix D. Compensated plots for the unified scaling $Nu \sim a^{-1}Re_{os}^{\beta}$

Figure 7 shows the compensated plots of the unified heat transport scaling law $Nu \sim a^{-1}Re_{os}^{\beta}$ with $\beta = 2$ in the TBL-dominant regime and $\beta = 4/3$ in the OBL-dominant regime using numerical data of both 3-D and 2-D cases, which correspond to figure 3. Those compensated plots shown in figure 7(*a–d*) further confirm the unified scaling laws we have obtained theoretically and numerically in the main text.

## References


Ahlers, G., *et al.* 2022 Aspect ratio dependence of heat transfer in a cylindrical Rayleigh–Bénard cell. *Phys. Rev. Lett.* **128** (8), 084501.

Ahlers, G., Grossmann, S. & Lohse, D. 2009 Heat transfer and large scale dynamics in turbulent Rayleigh–Bénard convection. *Rev. Mod. Phys.* **81** (2), 503–537.

Amiroudine, S. & Beysens, D. 2008 Thermovibrational instability in supercritical fluids under weightlessness. *Phys. Rev.* E **78** (3), 036325.

Apffel, B., Hidalgo-Caballero, S., Eddi, A. & Fort, E. 2021 Liquid walls and interfaces in arbitrary directions stabilized by vibrations. *Proc. Natl Acad. Sci. USA* **118** (48), e2111214118.

Apffel, B., Novkoski, F., Eddi, A. & Fort, E. 2020 Floating under a levitating liquid. *Nature* **585** (7823), 48–52.

Beysens, D. 2006 Vibrations in space as an artificial gravity? *Europhys. News* **37** (3), 22–25.

Beysens, D., Chatain, D., Evesque, P. & Garrabos, Y. 2005 High-frequency driven capillary flows speed up the gas–liquid phase transition in zero-gravity conditions. *Phys. Rev. Lett.* **95** (3), 034502.

Blass, A., Zhu, X., Verzicco, R., Lohse, D. & Stevens, R.J. 2020 Flow organization and heat transfer in turbulent wall sheared thermal convection. *J. Fluid Mech.* **897**, A22.

Brunet, P., Eggers, J. & Deegan, R.D. 2007 Vibration-induced climbing of drops. *Phys. Rev. Lett.* **99**, 144501.

Chen, X., Wang, D.-P. & Xi, H.-D. 2020 Reduced flow reversals in turbulent convection in the absence of corner vortices. *J. Fluid Mech.* **891**, R5.

CHONG, K.L., QIAO, S., WU, J.-Z. & WANG, B.-F. 2024 Heat transfer enhancement in vertical convection under spatially harmonic temperature modulation. *Intl J. Heat Mass Transfer* **227**, 125452.

CISSÉ, I., BARDAN, G. & MOJTABI, A. 2004 Rayleigh–Bénard convective instability of a fluid under high-frequency vibration. *Intl J. Heat Mass Transfer* **47** (19–20), 4101–4112.

CREWDSON, G. & LAPPA, M. 2021 Thermally-driven flows and turbulence in vibrated liquids. *Intl J. Thermofluids* **11**, 100102.

DANIEL, S., CHAUDHURY, M.K. & DE GENNES, P.-G. 2005 Vibration-actuated drop motion on surfaces for batch microfluidic processes. *Langmuir* **21** (9), 4240–4248.

ECKE, R.E. & SHISHKINA, O. 2023 Turbulent rotating Rayleigh–Bénard convection. *Annu. Rev. Fluid Mech.* **55**, 603–638.

GAPONENKO, Y., TORREGROSA, M., YASNOU, V., MIALDUN, A. & SHEVTSOVA, V. 2015 Interfacial pattern selection in miscible liquids under vibration. *Soft Matt.* **11** (42), 8221–8224.

GARRABOS, Y., BEYSENS, D., LECOUTRE, C., DEJOAN, A., POLEZHAEV, V. & EMELIANOV, V. 2007 Thermoconvectional phenomena induced by vibrations in supercritical $SF_6$ under weightlessness. *Phys. Rev.* E **75** (5), 056317.

GERSHUNI, G.Z. & LYUBIMOV, D.V. 1998 *Thermal Vibrational Convection*. Wiley & Sons.

GROSSMANN, S. & LOHSE, D. 2011 Multiple scaling in the ultimate regime of thermal convection. *Phys. Fluids* **23**, 045108.

GUO, X.-L., WU, J.-Z., WANG, B.-F., ZHOU, Q. & CHONG, K.L. 2023 Flow structure transition in thermal vibrational convection. *J. Fluid Mech.* **974**, A29.

GUO, X.-Q., WANG, B.-F., WU, J.-Z., CHONG, K.L. & ZHOU, Q. 2022 Turbulent vertical convection under vertical vibration. *Phys. Fluids* **34**, 055106.

HE, X., FUNFSCHILLING, D., NOBACH, H., BODENSCHATZ, E. & AHLERS, G. 2012 Transition to the ultimate state of turbulent Rayleigh–Bénard convection. *Phys. Rev. Lett.* **108** (2), 024502.

HIRATA, K., SASAKI, T. & TANIGAWA, H. 2001 Vibrational effects on convection in a square cavity at zero gravity. *J. Fluid Mech.* **445**, 327–344.

HUANG, Y.-X. & ZHOU, Q. 2013 Counter-gradient heat transport in two-dimensional turbulent Rayleigh–Bénard convection. *J. Fluid Mech.* **737**, R3.

HUANG, Z.-L., GUO, X.-L., WU, J.-Z., WANG, B.-F., CHONG, K.L. & ZHOU, Q. 2023 Rayleigh-number dependence of the critical vibration frequency in vibrating thermal turbulence. *Phys. Rev. Fluids* **8** (11), 113501.

IYER, K.P., SCHEEL, J.D., SCHUMACHER, J. & SREENIVASAN, K.R. 2020 Classical 1/3 scaling of convection holds up to $Ra = 10^{15}$. *Proc. Natl Acad. Sci. USA* **117** (14), 7594–7598.

JIANG, H., WANG, D., LIU, S. & SUN, C. 2022 Experimental evidence for the existence of the ultimate regime in rapidly rotating turbulent thermal convection. *Phys. Rev. Lett.* **129** (20), 204502.

JIANG, H., ZHU, X., WANG, D., HUISMAN, S.G. & SUN, C. 2020 Supergravitational turbulent thermal convection. *Sci. Adv.* **6** (40), eabb8676.

JIN, T.-C., WU, J.-Z., ZHANG, Y.-Z., LIU, Y.-L. & ZHOU, Q. 2022 Shear-induced modulation on thermal convection over rough plates. *J. Fluid Mech.* **936**, A28.

LEPOT, S., AUMAÎTRE, S. & GALLET, B. 2018 Radiative heating achieves the ultimate regime of thermal convection. *Proc. Natl Acad. Sci. USA* **115** (36), 8937–8941.

LI, Y.-Z., CHEN, X. & XI, H.-D. 2024 Enhanced heat transfer and reduced flow reversals in turbulent thermal convection with an obstructed centre. *J. Fluid Mech.* **981**, A16.

LI, Y.-Z., CHEN, X., XU, A. & XI, H.-D. 2022 Counter-flow orbiting of the vortex centre in turbulent thermal convection. *J. Fluid Mech.* **935**, A19.

MELNIKOV, D., RYZHKOV, I., MIALDUN, A. & SHEVTSOVA, V. 2008 Thermovibrational convection in microgravity: preparation of a parabolic flight experiment. *Microgravity Sci. Technol.* **20**, 29–39.

MENG, W.-S., ZHAO, C.-B., WU, J.-Z., WANG, B.-F., ZHOU, Q. & CHONG, K.L. 2024 Simulation of flow and debris migration in extreme ultraviolet source vessel. *Phys. Fluids* **36** (2), 023322.

MIALDUN, A., RYZHKOV, I., MELNIKOV, D. & SHEVTSOVA, V. 2008 Experimental evidence of thermal vibrational convection in a nonuniformly heated fluid in a reduced gravity environment. *Phys. Rev. Lett.* **101** (8), 084501.

MONTI, R., SAVINO, R. & LAPPA, M. 2001 On the convective disturbances induced by g-jitter on the space station. *Acta Astronaut.* **48** (5–12), 603–615.

PESCH, W., PALANIAPPAN, D., TAO, J. & BUSSE, F.H. 2008 Convection in heated fluid layers subjected to time-periodic horizontal accelerations. *J. Fluid Mech.* **596**, 313–332.

PLUMLEY, M. & JULIEN, K. 2019 Scaling laws in Rayleigh–Bénard convection. *Earth Space Sci.* **6** (9), 1580–1592.

ROGERS, J.L., SCHATZ, M.F., BOUGIE, J.L. & SWIFT, J.B. 2000*a* Rayleigh–Bénard convection in a vertically oscillated fluid layer. *Phys. Rev. Lett.* **84** (1), 87.

ROGERS, J.L., SCHATZ, M.F., BRAUSCH, O. & PESCH, W. 2000*b* Superlattice patterns in vertically oscillated Rayleigh–Bénard convection. *Phys. Rev. Lett.* **85** (20), 4281.

SALGADO SÁNCHEZ, P., GAPONENKO, Y.A., PORTER, J. & SHEVTSOVA, V. 2019 Finite-size effects on pattern selection in immiscible fluids subjected to horizontal vibrations in weightlessness. *Phys. Rev.* E **99**, 042803.

SÁNCHEZ, P.S., GAPONENKO, Y., YASNOU, V., MIALDUN, A., PORTER, J. & SHEVTSOVA, V. 2020 Effect of initial interface orientation on patterns produced by vibrational forcing in microgravity. *J. Fluid Mech.* **884**, A38.

SÁNCHEZ, P.S., YASNOU, V., GAPONENKO, Y., MIALDUN, A., PORTER, J. & SHEVTSOVA, V. 2019 Interfacial phenomena in immiscible liquids subjected to vibrations in microgravity. *J. Fluid Mech.* **865**, 850–883.

SAVINO, R., MONTI, R. & PICCIRILLO, M. 1998 Thermovibrational convection in a fluid cell. *Comput. Fluids* **27** (8), 923–939.

SCAGLIARINI, A., GYLFASON, Á. & TOSCHI, F. 2014 Heat-flux scaling in turbulent Rayleigh–Bénard convection with an imposed longitudinal wind. *Phys. Rev.* E **89** (4), 043012.

SHARMA, D., ERRIGUIBLE, A., GANDIKOTA, G., BEYSENS, D. & AMIROUDINE, S. 2019 Vibration-induced thermal instabilities in supercritical fluids in the absence of gravity. *Phys. Rev. Fluids* **4** (3), 033401.

SHEVTSOVA, V., RYZHKOV, I.I., MELNIKOV, D.E., GAPONENKO, Y.A. & MIALDUN, A. 2010 Experimental and theoretical study of vibration-induced thermal convection in low gravity. *J. Fluid Mech.* **648**, 53–82.

SREENIVASAN, K.R. 2019 Turbulent mixing: a perspective. *Proc. Natl Acad. Sci. USA* **116** (37), 18175–18183.

STEVENS, R.J., VAN DER POEL, E.P., GROSSMANN, S. & LOHSE, D. 2013 The unifying theory of scaling in thermal convection: the updated prefactors. *J. Fluid Mech.* **730**, 295–308.

SWAMINATHAN, A., GARRETT, S.L., POESE, M.E. & SMITH, R.W. 2018 Dynamic stabilization of the Rayleigh–Bénard instability by acceleration modulation. *J. Acoust. Soc. Am.* **144** (4), 2334–2343.

TOPPALADODDI, S., SUCCI, S. & WETTLAUFER, J.S. 2017 Roughness as a route to the ultimate regime of thermal convection. *Phys. Rev. Lett.* **118** (7), 074503.

WANG, B.-F., ZHOU, Q. & SUN, C. 2020 Vibration-induced boundary-layer destabilization achieves massive heat-transport enhancement. *Sci. Adv.* **6** (21), eaaz8239.

WANG, Z., CALZAVARINI, E., SUN, C. & TOSCHI, F. 2021 How the growth of ice depends on the fluid dynamics underneath. *Proc. Natl Acad. Sci. USA* **118** (10), e2012870118.

WANG, Z., MATHAI, V. & SUN, C. 2019 Self-sustained biphasic catalytic particle turbulence. *Nat. Commun.* **10**, 3333.

WU, J.-Z., DONG, Y.-H., WANG, B.-F. & ZHOU, Q. 2021 Phase decomposition analysis on oscillatory Rayleigh–Bénard turbulence. *Phys. Fluids* **33** (4), 045108.

WU, J.-Z., WANG, B.-F., CHONG, K.L., DONG, Y.-H., SUN, C. & ZHOU, Q. 2022*a* Vibration-induced 'anti-gravity' tames thermal turbulence at high Rayleigh numbers. *J. Fluid Mech.* **951**, A13.

WU, J.-Z., WANG, B.-F. & ZHOU, Q. 2022*b* Massive heat transfer enhancement of Rayleigh–Bénard turbulence over rough surfaces and under horizontal vibration. *Acta Mech. Sin.* **38**, 321319.

XI, H.-D., ZHANG, Y.-B., HAO, J.-T. & XIA, K.-Q. 2016 Higher-order flow modes in turbulent Rayleigh–Bénard convection. *J. Fluid Mech.* **805**, 31–51.

XU, A., XU, B.-R. & XI, H.-D. 2023 Wall-sheared thermal convection: heat transfer enhancement and turbulence relaminarization. *J. Fluid Mech.* **960**, A2.

ZHANG, Y. & ZHOU, Q. 2024 Low-Prandtl-number effects on global and local statistics in two-dimensional Rayleigh–Bénard convection. *Phys. Fluids* **36**, 015107.

ZHANG, Y., ZHOU, Q. & SUN, C. 2017 Statistics of kinetic and thermal energy dissipation rates in two-dimensional turbulent Rayleigh–Bénard convection. *J. Fluid Mech.* **814**, 165–184.

ZHANG, Y.-Z., SUN, C., BAO, Y. & ZHOU, Q. 2018 How surface roughness reduces heat transport for small roughness heights in turbulent Rayleigh–Bénard convection. *J. Fluid Mech.* **836**, R2.

ZHAO, C.-B., WANG, B.-F., WU, J.-Z., CHONG, K.L. & ZHOU, Q. 2022 Suppression of flow reversals via manipulating corner rolls in plane Rayleigh–Bénard convection. *J. Fluid Mech.* **946**, A44.

ZHAO, C.-B., WU, J.-Z., WANG, B.-F., CHANG, T., ZHOU, Q. & CHONG, K.L. 2024 Numerical study on the onset of global-scale flow from individual buoyant plumes: implications for indoor disease transmission. *Phys. Fluids* **36** (3), 035149.

ZOU, S. & YANG, Y. 2021 Realizing the ultimate scaling in convection turbulence by spatially decoupling the thermal and viscous boundary layers. *J. Fluid Mech.* **919**, R3.

ZYUZGIN, A., IVANOV, A., POLEZHAEV, V., PUTIN, G. & SOBOLEVA, E. 2001 Convective motions in near-critical fluids under real zero-gravity conditions. *Cosmic Res.* **39** (2), 175–186.